Probing Molecular and Crystalline Orientation in Solution-Processed Perovskite Solar Cells

Wenchao Huang, Fuzhi Huang, Eliot Gann, Yi-Bing Cheng, and Christopher R. McNeill**

The microstructure of solution-processed organometallic lead halide perovskite thin films prepared by the "gas-assisted" method is investigated with synchrotron-based techniques. Using a combination of GIWAXS and NEXAFS spectroscopy the orientational alignment of $CH_3NH_3PbI_3$ crystallites and $CH_3NH_3^+$ cations are separately probed. The GIWAXS results reveal a lack of preferential orientation of $CH_3NH_3PbI_3$ crystallites in 200–250 nm thick films prepared on both planar TiO_2 and mesoporous TiO_2. Relatively high efficiencies are observed for device based on such films, with 14.3% achieved for planar devices and 12% for mesoporous devices suggesting that highly oriented crystallites are not crucial for good cell performance. Oriented crystallites however are observed in thinner films (≈60 nm) deposited on planar TiO_2 (but not on mesoporous TiO_2) indicating that the formation of oriented crystallites is sensitive to the kinetics of solvent evaporation and the underlying TiO_2 morphology. NEXAFS measurements on all samples found that $CH_3NH_3^+$ cations exhibit a random molecular orientation with respect to the substrate. The lack of any NEXAFS dichroism for the thin $CH_3NH_3PbI_3$ layer deposited on planar TiO_2 in particular indicates the absence of any preferential orientation of $CH_3NH_3^+$ cations within the $CH_3NH_3PbI_3$ unit cell for as-prepared layers, that is, without any electrical poling.

1. Introduction

Harnessing energy from the sun is attracting increasing attention due to the challenges arising from our continued dependence on fossil fuels. Third-generation thin film solar cells such as organic photovoltaics,[1,2] dye sensitized solar cells,[3,4] and quantum dots solar cells[5,6] that are produced via solution processing have achieved efficiencies of up to 12%. However, raising efficiencies to levels comparable to crystalline silicon solar cells is urgently needed for viable commercialization. A viable candidate based on organolead trihalide perovskite light absorbing compounds has emerged in the past several years.[7–12] Owing to the high molar extinction coefficient[13] and long charge carrier diffusion length,[12,14–16] perovskite solar cells are able to efficiently utilize a p–i–n planar heterojunction structure. The active layer within this new type of solar cell is a thin layer of perovskite (e.g., $CH_3NH_3PbI_3$) which is typically sandwiched between a titanium dioxide electron transport layer and a hole-transport layer. The certified power conversion efficiency of these organic–inorganic hybrid solar cells has recently surpassed 20%.[17]

Perovskite solar cells are routinely fabricated by a low-cost solution process. Changes in the morphology of perovskite thin films during the solution process or post-treatments play an important role in determining overall device performance.[10,18–20] First, the organic $CH_3NH_3^+$ cation is a molecular dipole and the alignment of these cations is considered as a possible factor to explain the hysteresis phenomena of perovskite solar cells.[21,22] In addition to the alignment of the $CH_3NH_3^+$ cation, the crystal structure of the perovskite film is also important to device performance.[23–25] In perovskite solar cells, charge carrier transport within the device is in the vertical direction toward the electrodes. There exist different charge transport mobilities along the different crystallographic directions, meaning the performance of perovskite solar cells is expected to be sensitive to the degree of crystallinity, crystallite size, and crystalline orientation within the thin films.[26,27] The coverage of the perovskite layer is another crucial factor for the realization of high efficiency cells.[18] Defect pores in the active layer lead to severe charge recombination,[28] which is detrimental to device performance. Improved coverage of the perovskite layer has been successfully achieved by varying the thermal annealing temperature and time,[18] or through vapor assisted solution process.[29] In previous studies, it has been found that control of the heterogeneous nucleation rate is a promising way to prepare a uniform and fully covered active layer.[28,30] In particular, our previous study reported that rapid removal of solvent during the spin-coating process to increase the density of nucleation sites yields high efficiency devices with excellent film quality.[28]

W. Huang, Dr. F. Huang, Dr. E. Gann,
Prof. Y.-B. Cheng, Assoc. Prof. C. R. McNeill
Department of Materials Science and Engineering
Monash University
Wellington Road, Clayton, VIC 3800, Australia
E-mail: yibing.cheng@monash.edu;
christopher.mcneill@monash.edu
Dr. E. Gann
Australian Synchrotron
800 Blackburn Road
Clayton, VIC 3168, Australia

DOI: 10.1002/adfm.201502553

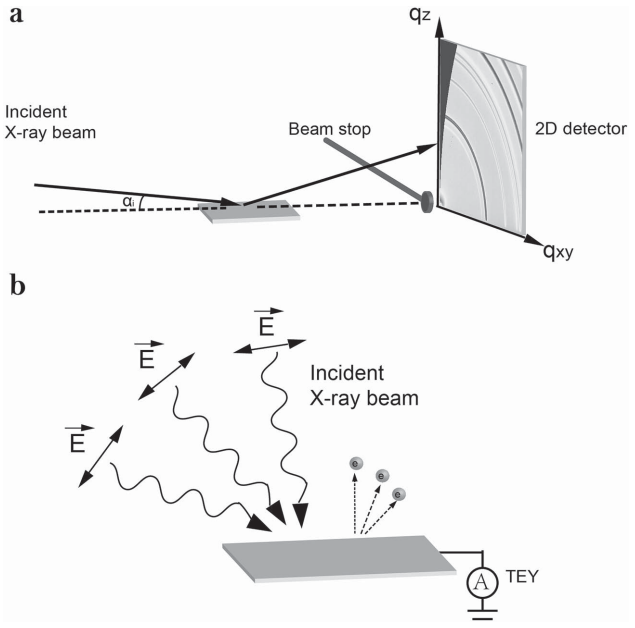

Figure 1. Schematic diagram of a) GIWAXS experimental setup and b) NEXAFS experimental setup.

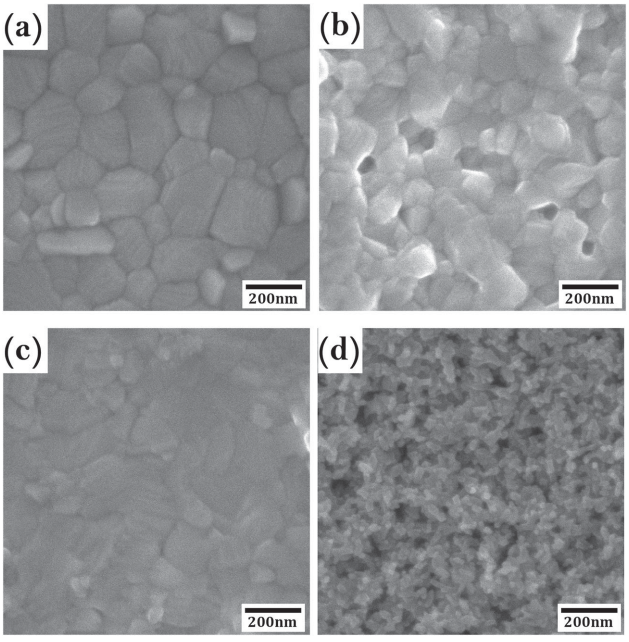

Figure 2. SEM images of perovskite layer prepared on planar TiO_2 a,c) and on mesoporous TiO_2 b,d). The films (a,b) were spin-coated from the solution with a concentration of 40 wt% and the films (c,d) were spin-coated from the solution with a concentration of 10 wt%. The films were heated at 100 °C for 10 min after spin coating.

Although the efficiency of perovskite solar cells has experienced a rapid increase over the past several years, the lack of morphological understanding is a potential obstacle to designing higher efficiency devices. In this study, by using a combination of advanced techniques, we aim at providing an in-depth understanding of the perovskite thin film microstructure. The orientation of methylammonium lead tri-iodide $CH_3NH_3PbI_3$ perovskite crystallites within the active layer is first characterized by grazing-incidence wide-angle X-ray scattering (GIWAXS), see **Figure 1**a. The use of high-flux synchrotron X-rays provides sufficient scattering signal in the planes parallel and perpendicular to the substrate with scattering patterns collected on a 2D detector. GIWAXS is therefore able to provide information not only about $CH_3NH_3PbI_3$ crystal packing but also about crystallite orientation with respect to the substrate. Second, the orientation of $CH_3NH_3^+$ cations within the perovskite layer is probed with near-edge X-ray absorption fine structure (NEXAFS) spectroscopy. Due to the linear polarization of synchrotron X-rays, the acquisition of NEXAFS spectra at different incident X-ray angles can be used to determine the ensemble-averaged orientation of molecular bonds such as the carbon–nitrogen sigma bond as shown schematically in Figure 1b.[31,32] Since NEXAFS spectroscopy probes molecular orientation with respect to the substrate, the combined application of GIWAXS and NEXAFS spectroscopy enables information regarding the orientation of the $CH_3NH_3^+$ cations within the $CH_3NH_3PbI_3$ unit cell to be inferred.

In this paper, GIWAXS and NEXAFS spectroscopy are employed to probe crystalline and molecular orientation in perovskite layers of different thickness prepared on both planar and mesoporous TiO_2 layers. In this way the influence of substrate morphology, film thickness, and the kinetics of solvent evaporation on the morphology of perovskite films have been studied. Device efficiencies of cells prepared using the same precursor solutions and processing conditions are also reported.

2. Results and Discussion

Perovskite layers were prepared by spin-coating different concentrations (10 and 40 wt%) of $CH_3NH_3PbI_3$ in dimethylformamide (DMF) solution on either planar or mesoporous TiO_2 via the gas-assisted method.[33] In this method, a stream of nitrogen gas is applied to the film during spin-coating, promoting rapid supersaturation and precipitation, and the formation of a smooth film comprised of densely packed grains of the alkylammonium lead iodide perovskite material. The thickness of the flat and mesoporous TiO_2 layers used in this study were ≈40 and ≈180 nm, respectively. It was found that the perovskite film prepared from the 40 wt% precursor solution on planar and mesoporous TiO_2 had a similar morphology, as shown in **Figure 2**a,b (see also low magnification images shown in Figure S1, Supporting Information). In general, this similarity in morphology for the different underlying TiO_2 layers is likely due to the formation of a capping layer of perovskite on the top of the mesoporous TiO_2/perovskite layer.[34] Such a capping layer (with a thickness of ≈200 nm) overlying the TiO_2 scaffold is quite similar to the perovskite film directly deposited on the planar TiO_2 layer (thickness of ≈250 nm). This is to say, it is expected that underlayer effects on the film morphology are less likely to be important in thicker films. These thicker perovskite films prepared from the 40 wt% solution have a uniform coverage on TiO_2 with crystallite sizes of ≈250 nm. In order to investigate the morphology of perovskite close to the

interface between perovskite film and the TiO_2 layer, very thin films of the perovskite were spin-coated from a low concentration solution (10 wt%). In the planar architecture (Figure 2c), the flat TiO_2 is fully covered by the perovskite active layer (with a thickness of ≈60 nm) with a slightly smaller crystallite size of ≈150 nm. In contrast, a significant difference in morphology is found for the mesoporous architecture with the surface morphology dominated by the mesoporous TiO_2, see Figure 2d. In particular, for the thin perovskite film deposited on the mesoporous TiO_2 layer, the perovskite solution appears to have filled the TiO_2 pores during spin-coating, with the lack of a continuous perovskite capping layer. X-ray photoelectron spectroscopy (XPS, see Figure S2, Supporting Information) measurements confirm the lack of a complete coverage of the mesoporous TiO_2 layer, with titanium 2p and oxygen 1s peaks both prominent. In contrast, for the thick sample on mesoporous TiO_2 and for the thin film on planar TiO_2 both Ti 2p and O 1s peaks are absent, indicating complete coverage of the underlying TiO_2 layers.

To investigate the crystalline nature of these solution-processed CH_3NH_3PbI thin films, 2D scattering patterns were recorded with synchrotron-based GIWAXS, revealing not only information regarding crystalline lattice parameters but also information regarding thin-film crystallinity and crystallite orientation. GIWAXS has been widely employed to investigate organic semiconductor thin films[33,35–37] and is emerging as an important technique for characterizing perovskite thin films.[23,25,38] The GIWAXS results of perovskite thin films deposited on different substrates and with different film thicknesses are compared in **Figure 3** and are qualitatively similar to previous GIWAXS studies.[23,25,38] The 2D scattering patterns are shown in Figure 3a–d while out-of-plane (OOP) and in-plane (IP) line profiles extracted from these 2D scattering patterns are shown in Figure 3e,f. Figure S3 of the Supporting Information illustrates the integration area used for the OOP and IP profiles. The intense peak observed at $q = 0.98$ Å^{-1} corresponds to the $CH_3NH_3PbI_3$ (110) peak which will be primarily used to assess crystalline orientation. For highly oriented $CH_3NH_3PbI_3$ crystallites, increased scattering intensity of this peak either out of plane (along the Q_z axis) or in plane (along the Q_{xy}) axis is expected. For the case where there is no preferential orientation of the $CH_3NH_3PbI_3$ crystal axes with respect to the substrate, a uniform scattering intensity of the (110) peak about the ring corresponding to $q = 0.98$ Å^{-1} is expected.

First, the effects of film thickness are investigated for the planar TiO_2 substrate (Figure 3a,c). For the thicker film prepared by the gas-assisted method, which corresponds to the optimum thickness used in devices, the scattering pattern of the $CH_3NH_3PbI_3$ (110) peak exhibits a uniform halo shape,

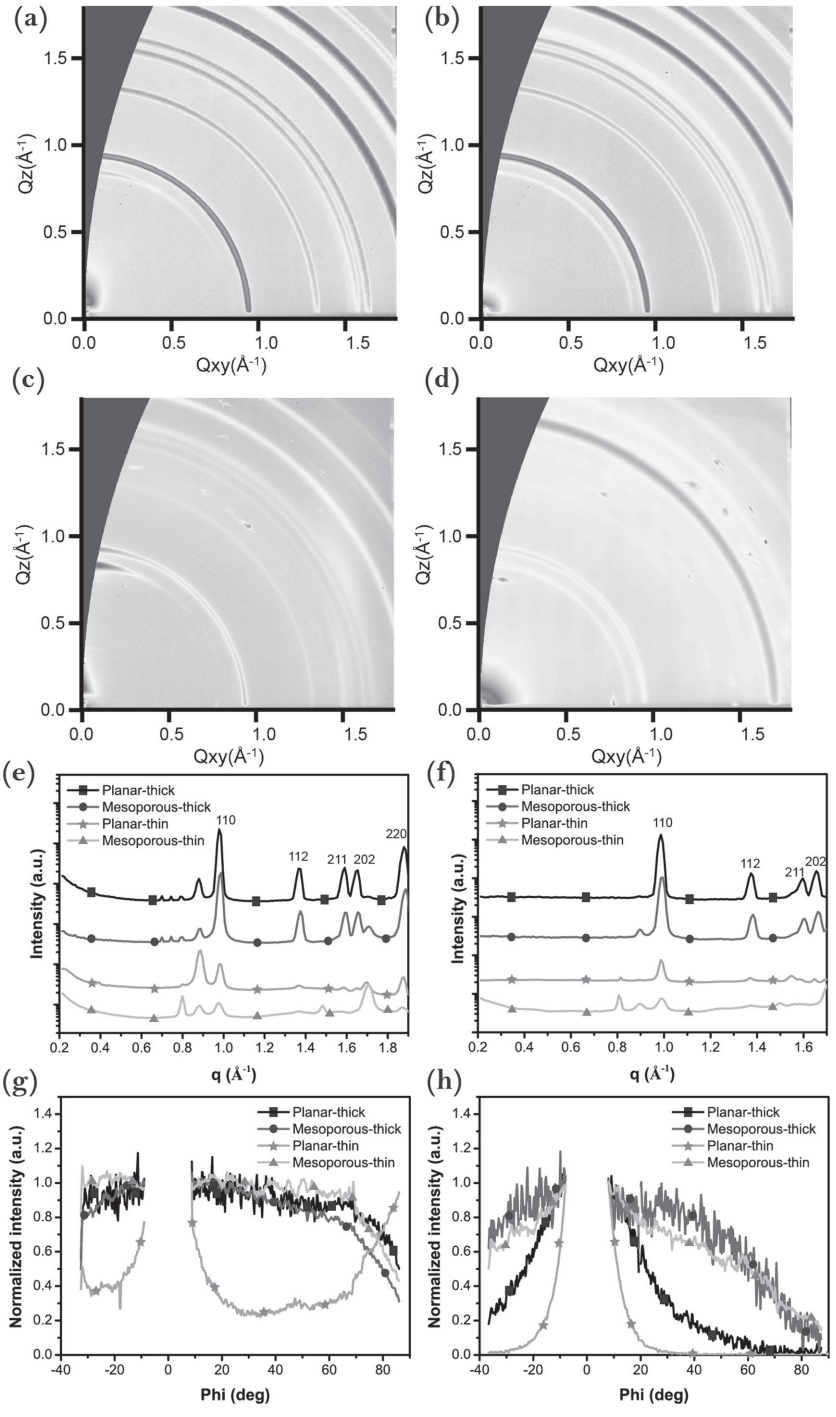

Figure 3. 2D GIWAXS patterns of perovskite films prepared a,c) on planar TiO_2 and b,d) on mesoporous TiO_2. a,b) Films spin-coated from a solution with concentration of 40 wt%. c,d) Films spin-coated from a solution with concentration of 10 wt%. e) Out-of-plane GIWAXS line profiles. f) In-plane GIWAXS line profiles. g) Pole figures of the $CH_3NH_3PbI_3$ (110) peak. h) Pole figures of the PbI_2 (001) peak.

while for the thin film more intense scattering is observed closer to the Q_z and Q_{xy} axes. The partial pole figure of the $CH_3NH_3PbI_3$ (110) peak is plotted in Figure 3g which plots the intensity of the (110) peak as a function of azimuthal angle. It is noted that polar angles lower than the scattering angle are impossible to record in the grazing angle geometry, resulting in the missing wedge in the 2D scattering patterns. The weak azimuthal angle dependency of the (110) peak intensity in the thicker film indicates a random orientation of crystallites. However, in the thin film spin-coated from the low concentration solution (also prepared via the gas-assisted method), the peak intensity close to 90° (OOP) or 0° (IP) is significantly higher than the intensity at 45°. As shown in Table S1 of the Supporting Information, the s-value (Herman's oreintation parameter) calculated from the out of plane distribution is 0.93, indicating a strong preferential orientation of the $CH_3NH_3PbI_3$ crystallites with respect to the substrate for the thin film prepared on the planar TiO_2 layer (an s-value of 1 corresponds to perfectly oriented crystallites, with randomly oriented crystallites giving an s-vlaue of 0).

Second, we observe how the underlying TiO_2 morphology influences the thin-film perovskite microstructure. For the perovskite layers prepared on mesoporous TiO_2 the position of the $CH_3NH_3PbI_3$ (110) peak is located at the same position as for the planar architecture structure, indicating that the crystallites have the same lattice parameters regardless of the substrate. From the pole figure, both thick and thin perovskite films on the mesoporous TiO_2 show a random crystallite orientation similar to the thicker film on planar TiO_2. Thus the preferential orientation observed for the thin film on the planar TiO_2 is not preserved in the thin film on mesoporous TiO_2. During the perovskite deposition process, the crystals nucleate at the surface of the TiO_2 followed by grain growth. Because of the need to minimize the free energy of the interface between perovskite and TiO_2, the nucleation and growth of perovskite crystallites is strongly dependent on the morphology of underlying layer, particularly in the thin film. In the planar architecture, the perovskite film shows good coverage with crystal growth initially templated by the flat TiO_2. In contrast, the perovskite film in the mesoporous architecture is integrated into a mesoporous network of TiO_2. The morphology of two different types of TiO_2 is also investigated in Figure S4 of the Supporting Information. Compared with flat TiO_2, the orientation of TiO_2 crystallites in the mesoporous structure shows a more random distribution, which leads to disordered crystallite orientation in the perovskite active layer.

It is also observed that the presence of crystalline PbI_2 is sensitive to the substrate type. As shown in 2D scattering patterns, the peak located at $q = 0.88$ Å^{-1} is identified as the PbI_2 (001) peak. It is worth noting that a higher concentration of PbI_2 has been detected in the planar structure by integrating the intensity from azimuthal angles between 0° and 90°, indicating that the perovskite film on the planar TiO_2 shows a higher tendency to decompose into PbI_2. In addition, as shown in the pole figure of the PbI_2 (001) peak (Figure 3h), the PbI_2 (001) direction in the planar architecture is highly aligned out-of-plane, while this peak shows a relatively random orientational distribution in the mesoporous architecture. Moreover, regardless of the architecture, a higher PbI_2 peak intensity is always observed in thin perovskite films, suggesting that perovskite degradation is more rapid in thinner perovskite films, consistent with the conclusion of a previous study.[25]

Third, we observe that the solvent evaporation rate plays an important role in tuning the morphology of the perovskite active layer. Two different spin-coating methods, in particular the conventional spin-coating method and gas-assisted have been compared. In the gas-assisted method, solvent is quickly removed with the assistance of nitrogen gas, which significantly increases the nucleation rate at the expense of the crystallite growth rate. Hence, the thicker film prepared by the gas-assisted method shows uniaxial grains with excellent surface coverage, but poor crystallite orientation. On the other hand, the conventional spin-coating method affords a longer time for $CH_3NH_3PbI_3$ crystals to grow into a dendritic morphology of oriented crystallites (Figure S5a, Supporting Information). Due to a slow solvent evaporation rate, the formation of a dendritic morphology leads to a poor surface coverage, but the (110) plane of perovskite crystallite is aligned in the direction perpendicular or parallel to the planar TiO_2, as shown in Figure S5b–d of the Supporting Information. Thus while the gas-assisted method is effective in providing a superior surface coverage and film uniformity it comes at the expense of a random crystallite orientation.

NEXAFS spectroscopy measures the X-ray absorption spectrum of a material enabling identification of resonant electronic transitions from a core state to antibonding molecular orbitals. The total electron yield (TEY) mode which was used in this study affords a surface sensitivity of <5 nm. NEXAFS spectra were acquired at five different incident angles (20°, 40°, 55°, 70°, and 90°), varying the incident angle from glancing (20°) to normal (90°) incidence. **Figure 4** presents the carbon K-edge NEXAFS spectra of perovskite films prepared in a similar fashion to those in Figure 1. The NEXAFS spectra of the perovskite films are dominated by peaks at ≈288 and ≈290 eV which are attributed to transitions of C–H and C–N σ^* bonds, respectively.[32] Intriguingly there is a weak peak located at ≈285 eV (more prominent in the thin perovskite film of the mesoporous TiO_2 layer), an energy traditionally associated with transitions to π^* orbitals of which there are expected to be none in the material investigated. In any case, very little dichroism is observed for all samples consistent with a lack of preferential orientation of methyl ammonium cations with respect to the substrate. Nitrogen edge spectra (see Figure S6, Supporting Information) also show no dichroism confirming the observations made at the carbon edge. Therefore, we conclude that in as-prepared films (that is, films that have not been subject to any electrical poling in a device structure) there is no preferential orientation of the $CH_3NH_3^+$ cations with respect to the substrate. Combined with our GIWAXS observations above that found a preferential orientation of the perovskite unit cell for the case of the thin perovskite layer on the planar substrate, these two results taken together indicate the lack of a preferential orientation of $CH_3NH_3^+$ cations within the perovskite unit cell, at least in as-prepared layers that have not been subject to poling.

Interestingly, our results are in stark contrast to those of McLeod et al. who recently reported NEXAFS observations of perovskite layers.[39] In particular McLeod et al. observed

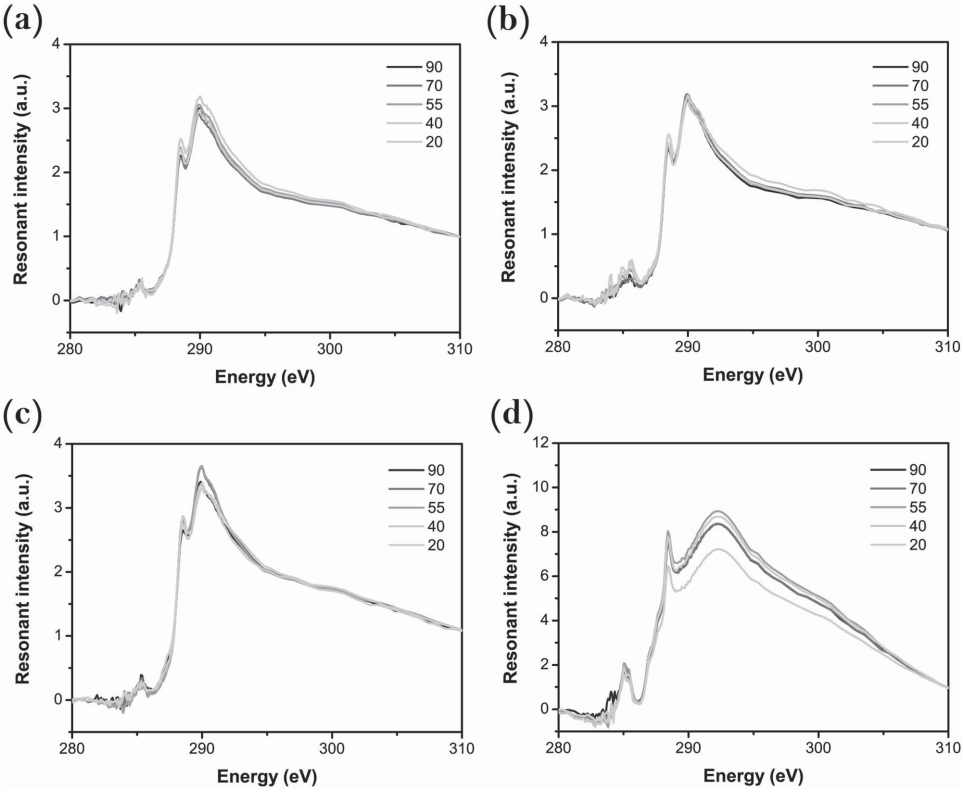

Figure 4. Angle-resolved carbon K-edge NEXAFS spectra of perovskite layers prepared on a,c) planar TiO_2 and on b,d) mesoporous TiO_2. In (a,b) The films were spin-coated from a solution with concentration of 40 wt% and in (c,d) the films were spin-coated from a solution with concentration of 10 wt%.

a strong peak located at ≈285 eV with associated strong dichroism, with McLeod et al. taking this as evidence for self-alignment of the methylammonium cations (although preferential orientation of the perovskite crystalline axes was not confirmed). The presence of a strong peak at 285 eV and strong dichroism in their work are in contrast to our observations where we see only a weak oscillator strength at 285 eV and no apparent dichroism. In their paper, McLeod et al. tentatively assigned their observed peak at 285 eV to a C–N σ^* bond, however the C–N σ^* resonance is reported to be 291.5 eV.[32] From our observations, increased resonance intensity at 285 eV can be associated with beam damage and adventitious carbon. By acquiring consecutive scans of the same position on a perovskite sample, we find that this repeated scanning results in an increase in the intensity of the peak at 285 eV (see Figure S7, Supporting Information) which can be attributed to beam damage, or X-ray-assisted deposition or carbon onto the sample. Furthermore, we observe a stronger resonance intensity at 285 eV for the thin perovskite layer on mesoporous TiO_2 for which the underlying substrate is exposed. Carbon contamination of the underlying substrate therefore provides another avenue for an anomalous peak at 285 eV. Finally, measurements at the carbon edge can be affected by carbon contamination of X-ray optics; if the acquired spectra are not properly normalized to account for carbon absorption from beam optics anomalous peaks may also result.[40] As our experiments have been performed on films with complete surface coverage (in the case of the thicker films), and have been performed under ultrahigh vacuum (pressure ≈10^{-10} mbar) on a beamline with only a 30% dip in X-ray intensity at the carbon edge, we are confident that the spectra we measure are representative of the true NEXAFS spectra of photovoltaic perovskite layers. (We note that the perovskite material appears to be stable in ultra-high vacuum (UHV). From XPS survey scans taken in UHV at the time of the NEXAFS measurements we have determined the atomic ratio of C:Pb:I to be 0.96:1:3.07, which is close to the anticipated value of 1:1:3. This indicates that there is minimal sublimation of the methyl ammonium ions in UHV.)

We are reluctant to attribute the weak resonance intensity that we do observe at 285 eV entirely to beam damage or contamination. Using bulk-sensitive fluorescence yield measurements (see Figure S8, Supporting Information) we also observe a weak peak at 285 eV. Due to the different nature of fluorescence yield measurements (bulk sensitive, not affected by surface contamination, different sensitivity to beam damage) we are of the opinion that the small peak we observe at 285 eV may indeed be genuine. The origin of this peak is uncertain, and note that the NEXAFS spectra of ionic materials such as $CH_3NH_3^+$ are not commonly reported.

In order to establish that our morphological characterization reflects functional perovskite layers, devices have been fabricated using the same batch of the precursor solution and film deposition protocols (these devices are based on the "thicker" layers as shown in Figure 2). Devices fabricated by the gas-assisted method show excellent photovoltaic performance for both planar and mesoporous architectures. **Figure 5** shows the

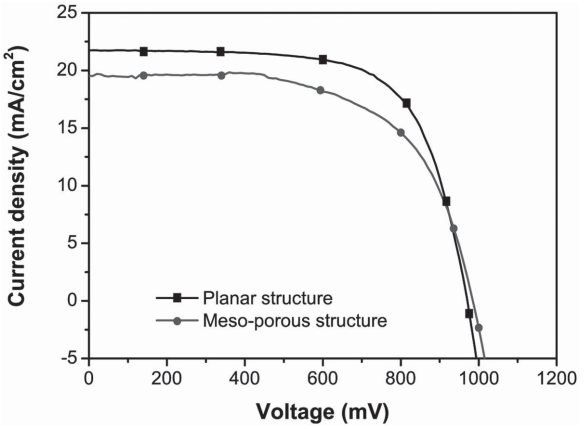

Figure 5. Current–voltage characteristics of perovskite solar cells based on planar and mesoporous structures. The active perovksite layers (200–250 nm thick) were prepared with the gas-assisted method.

current–voltage (*J*–*V*) characteristics under AM1.5 one sun with a light intensity of 100 mW cm^{-2}. (The forward and reverse bias scans are presented in Figure S9, Supporting Information.) Details of device performance are summarized in **Table 1**. The device fabricated in a planar structure shows an efficiency of 14.3% with a short-circuit current of 21.7 mA cm^{-2}, an open-circuit voltage of 0.97 V and a fill factor of 0.68. The device constructed on a mesoporous TiO_2 exhibits a slightly poorer performance, yielding an efficiency of 12.0% with a short-circuit current of 19.5 mA cm^{-2}, an open-circuit voltage of 0.98 V and a fill factor of 0.63. On the other hand, the device prepared with the conventional spin-coating method is also characterized in Figure S10 of the Supporting Information exhibiting a poor efficiency of only 2.9%, similar to our previous reported value.[28,41] We note that this conventionally spin-coated device is far from optimised but is presented as a useful comparison of how a poor photovoltaic performance is achieved for the same batch of material if uniform surface coverage is not achieved.

In this study, we have investigated several factors including film thickness, the morphology of underlying TiO_2 layer, and solvent evaporation rate on the resulting thin-film perovskite microstructure. For the planar architecture (prepared by the gas-assisted method), highly orientated crystallites are observed in the thin perovskite film with this preferential orientation disappearing for thicker (250 nm thick) films as used in optimised solar cells. In contrast, for films prepared on mesoporous TiO_2, both thin and thick perovskite films exhibit a random crystallite orientation. These observations indicate that the underlying substrate can template the alignment of crystallites during solvent evaporation provided the quenching rate is not too high. In concert with the GIWAXS measurements, NEXAFS measurements that separately probe the molecular orientation of $CH_3NH_3^+$ cations found no evidence of molecular alignment, either with respect to the substrate or (in the case of the thin film on planar TiO_2) within the unit cell of the perovskite crystal.

Table 1. Photovoltaics performance of the perovskite solar cells based on planar structure and mesoporous structure.

Device	J_{sc} [mA cm^{-2}]	V_{oc} [V]	Fill factor	Efficiency [%]
Planar structure	21.7	0.97	0.68	14.3
Mesoporous structure	19.5	0.98	0.63	12.0

Films prepared by the gas-assisted method and with the conventional spin-coating method were also compared in this study. In the film prepared by the gas-assisted method, the fast kinetics of solvent evaporation forms a uniform film. However, due to the strain from rapid nucleation and neighboring grains, the crystallites have difficulty reorganizing to a preferential orientation. Therefore, the thicker perovskite film on flat TiO_2 loses a preferential orientation of crystallites. On the other hand, films spin-coated without gas-assistance show a highly preferential orientation even in the thick film. Despite the poor surface coverage, the dendritic morphology provides enough free space for perovskite crystallites to grow along a certain direction and the slow solvent evaporation rate provides enough time for crystalline reorganization.

Although conventionally spin-coated perovskite films exhibit a higher level of crystallite alignment, devices prepared on such layers show a poor photovoltaic performance (see Figure S8, Supporting Information). The poor device performance observed in the conventionally prepared device is attributed to poor surface coverage. The dendritic morphology of the perovskite allows direct contact between the hole-transport layer and TiO_2, which results in low shunt resistance, and precludes high performance despite other beneficial morphological factors including crystalline alignment, which is confirmed by previous work.[18,24]

Regarding the importance of crystalline orientation, it is useful to compare our results to those of Saliba et al. who characterized the microstructure and solar cell performance of methylammonium lead mixed halide ($CH_3NH_3PbI_{3-x}Cl_x$) perovskite layers.[24] Through the application of a short rapid thermal annealing at 130 °C subsequent to spin-coating, Saliba et al. were able to produce layers with highly oriented crystallites (as evidenced by GIWAXS observations) with good surface coverage. The reported power conversion efficiencies of devices based on flash annealing showed an average efficiency of 10.7% compared to 9.9% for the conventionally annealed films that exhibited a lack of crystalline orientation. Taken together with our results it appears that the performance of thin-film perovskite solar cells is not overly sensitive to the degree of orientational order, with good photovoltaic performance achievable for layers with a random orientation of crystallites. Although highly oriented crystallites might be required to achieve record lab-based efficiencies, the ability to achieve good photovoltaic performance with a random crystallite orientation should be regarded as a positive result from a manufacturing perspective, where high tolerances for various material parameters is desired. In addition to surface coverage and crystalline orientation, other factors beyond the scope of this study such as grain size and grain boundaries are also key factors. One could expect that for a fixed film thickness, having a random crystallite orientation will limit the domain size to being of order of the film thickness. Thus grain size and crystallite orientation may be expected to be linked. We anticipate that the development of post-deposition treatments to tune the orientation and grain

size of perovskite crystallites post-film formation could be an effective strategy to combine the benefits of a uniform surface coverage achieved with the gas-assisted method with an extra efficiency boost associated with oriented (and larger) grains.

3. Conclusions

In summary, we have used a combination of GIWAXS and NEXAFS spectroscopy to probe crystalline and molecular orientation in solution-processed $CH_3NH_3PbI_3$ films produced by the gas-assisted method. Using GIWAXS the morphology of $CH_3NH_3PbI_3$ crystallites has been linked to the underlying TiO_2 morphology, film thickness and kinetics of solvent evaporation. Combined with the GIWAXS observations, the NEXAFS results indicate a lack of preferential orientation of $CH_3NH_3^+$ cations with respect to the substrate and within the $CH_3NH_3PbI_3$ unit cell of as-prepared layers. Despite the random orientation of crystallites in thicker films used in devices prepared by the gas-assisted method, good efficiencies of 14.3% and 12.0% were still realized in planar and mesoporous structures, respectively, indicating a limited sensitivity of cell performance to crystallite orientation.

4. Experimental Section

Materials: Unless specified otherwise, all materials were purchased from either Alfa Aesar or Sigma-Aldrich. Spiro-MeOTAD was supplied by Luminescence Technology Corp. The synthesis of $CH_3NH_3PbI_3$ has been based on our previous paper.[28]

Device Fabrication: Patterned FTO glass was first consecutively washed with detergent, deionized water, and isopropanol. A TiO_2 blocking layer was deposited on the cleaned FTO glass by spray pyrolysis of the precursor bis(isopropoxide)-bis(acetylacetonate)titanium(IV) solution (this precursor solution was diluted in anhydrous isopropanol with the volume ratio of 1:9) at 450 °C. For the planar device, the perovskite layer was directly deposited on dense TiO_2 blocking layer, while for the mesoporous device, an additional mesoporous TiO_2 layer was coated on the top of the TiO_2 blocking layer by spin-coating of a TiO_2 slurry (CCIC NSD30 diluted with ethanol in 1:4 by weight) at a speed of 5000 rpm for 30 s.

The $CH_3NH_3PBI_3$ solutions were prepared in DMF by mixing CH_3NH_3I and PbI_2 in a molar ratio of 1:1. The concentrations of $CH_3NH_3PbI_3$ solutions used for fabricating the perovskite films were 40 wt% for the thick films and 10 wt% for the thin films. The perovskite layers were fabricated by the gas-assisted spin-coating method, reported in our previous study.[39] A 25 µL $CH_3NH_3PbI_3$ solution was spread on the substrate; the substrate was then spun at 6500 rpm. A 40 psi dry nitrogen gas stream was blown onto the substrate 2 s after spin-coating was started. The distance between the gas gun and the substrate was set at 3 cm. The gas flow was removed after 10 s and the substrate was spun for a further 18 s. The films were then annealed at 100 °C for 10 min, followed by cooling to room temperature. The solutions for the hole-transporting layer were prepared by dissolving 41.6 mg spiro-OMeTAD, 7.5 µL of a stock solution of 520 mg mL^{-1} lithium bis(trifluoronethylsulphonyl)imide in acetonitrile and 16.9 µL 4-tert-butylpyridine in 0.5 mL chlorobenzene. This solution was deposited on the perovskite film by spin-coating at 3000 rpm for 30 s. An 80 nm Au electrode was thermal-evaporated atop the hole-transporting layer.

Characterization: PV Performance: The current–voltage (*J–V*) curve was measured under 100 mW cm^{-2} by using an Oriel solar simulator with an AM1.5 filter. The intensity of simulated sun light was calibrated by a standard silicon diode. The active area of device was defined by using a black metal mask with an aperture area of 0.16 cm^2. Incident photon to converted electron (IPCE) spectra were detected by dispersing light from a 300 W xenon lamp through an Oriel Cornerstone 260 ¼ m monochromator. The short-circuit current at each wavelength was recorded by a Keithley 2400 source meter.

GIWAXS: The samples prepared for synchrotron experiments were spin-coated on silicon wafers coated with either a compact or mesoporous TiO_2 layer to match device conditions. GIWAXS was collected at the SAXS/WAXS beamline at Australian Synchrotron.[42] The energy of X-ray incident beam was fixed at 9 keV with an incident angle of 0.50°. 2D scattering patterns were collected by a Dectris Pilatus 1M with a total exposure time of 3 s. The sample was moved to a new spot for each exposure. The scattering results were analysed by an altered version of NIKA analysis package.[43]

NEXAFS and XPS: The NEXAFS spectra and XPS were measured at the soft X-ray (SXR) beamline at the Australian Synchrotron.[44] Nearly perfectly linearly polarized photons were produced from an APPLE II elliptical polarized undulator with high spectral resolution. In NEXAFS experiments, the carbon edge spectra and nitrogen edge spectra were collected in a scan from 280 to 310 eV and 390 to 430 eV, respectively. TEY was measured as the drain current flux to the sample. The spectra were normalized by the "stable monitor method," followed by background subtraction and then normalized to 1 at 310 eV and 0 at 280 eV for carbon edge, and 1 at 430 eV and 0 at 390 eV for nitrogen edge and the photon energy was calibrated by measuring the NEXAFS spectra of pyrolytic graphite at the same time, similar to our previous studies. In order to avoid beam damage, the sample was moved to a new spot after each scan. In XPS measurements, an X-ray energy of 1486.7 eV was used and photoelectrons were detected using a SPECS phoibos 150 Hemispherical Analyzer with a pass energy of 40 eV.

SEM: The surface morphology of perovskite films were examined by using an FEI Nova NanoSEM 450 microscope without any additional conductive coating.

Supporting Information

Supporting Information is available from the Wiley Online Library or from the author.

Acknowledgements

W.H. and F.H. contributed equally to this work. NEXAFS spectroscopy and GIWAXS experiments were performed at soft X-ray and SAXS/WAXS beamlines at the Australian Synchrotron, Victoria, Australia. Support from the Australian Renewable Energy Agency (ARENA) and the Australian Centre for Advanced Photovoltaics (ACAP) is acknowledged. The authors also acknowledge Monash University Centre for Electron Microscopy (MCEM) for electron microscopy facilities. C.R.M acknowledges support from the Australian Research Council (FT100100275) and veski.

Received: June 22, 2015
Published online: August 4, 2015

[1] Z. He, B. Xiao, F. Liu, H. Wu, Y. Yang, S. Xiao, C. Wang, T. P. Russell, Y. Cao, *Nat. Photonics* **2015**, *9*, 174.
[2] Y. Liu, J. Zhao, Z. Li, C. Mu, W. Ma, H. Hu, K. Jiang, H. Lin, H. Ade, H. Yan, *Nat. Commun.* **2014**, *5*, 5293.
[3] B. O'Regan, M. Grätzel, *Nature* **1991**, *353*, 737.
[4] A. Hagfeldt, G. Boschloo, L. Sun, L. Kloo, H. Pettersson, *Chem. Rev.* **2010**, *110*, 6595.
[5] A. J. Nozik, *Physica E* **2002**, *14*, 115.

[6] E. H. Sargent, J. A. Tang, *Adv. Mater.* **2011**, *23*, 12.
[7] A. Kojima, K. Teshima, Y. Shirai, T. Miyasaka, *J. Am. Chem. Soc.* **2009**, *131*, 6050.
[8] J.-H. Im, C.-R. Lee, J.-W. Lee, S.-W. Park, N.-G. Park, *Nanoscale* **2011**, *3*, 4088.
[9] M. M. Lee, J. Teuscher, T. Miyasaka, T. N. Murakami, H. J. Snaith, *Science* **2012**, *338*, 643.
[10] J. Burschka, N. Pellet, S. J. Moon, R. Humphry-Baker, P. Gao, M. K. Nazeeruddin, M. Grätzel, *Nature* **2013**, *499*, 316.
[11] H. Zhou, Q. Chen, G. Li, S. Luo, T.-b. Song, H.-S. Duan, Z. Hong, J. You, Y. Liu, Y. Yang, *Science* **2014**, *345*, 542.
[12] D. Shi, V. Adinolfi, R. Comin, M. Yuan, E. Alarousu, A. Buin, Y. Chen, S. Hoogland, A. Rothenberger, K. Katsiev, Y. Losovyj, X. Zhang, P. A. Dowben, O. F. Mohammed, E. H. Sargent, O. M. Bakr, *Science* **2015**, *347*, 519.
[13] H. S. Kim, J. W. Lee, N. Yantara, P. P. Boix, S. A. Kulkarni, S. Mhaisalkar, M. Grätzel, N. G. Park, *Nano Lett.* **2013**, *13*, 2412.
[14] Q. Dong, Y. Fang, Y. Shao, P. Mulligan, J. Qiu, L. Cao, J. Huang, *Science* **2015**, *347*, 967.
[15] S. D. Stranks, G. E. Eperon, G. Grancini, C. Menelaou, M. J. P. Alcocer, T. Leijtens, L. M. Herz, A. Petrozza, H. J. Snaith, *Science* **2013**, *342*, 341.
[16] G. Xing, N. Mathews, S. Sun, S. S. Lim, Y. M. Lam, M. Grätzel, S. Mhaisalkar, T. C. Sum, *Science* **2013**, *342*, 344.
[17] M. A. Green, K. Emery, Y. Hishikawa, W. Warta, E. D. Dunlop, *Prog. Photovolt. Res. Appl.* **2015**, *23*, 1.
[18] G. E. Eperon, V. M. Burlakov, P. Docampo, A. Goriely, H. J. Snaith, *Adv. Funct. Mater.* **2014**, *24*, 151.
[19] M. Xiao, F. Z. Huang, W. Huang, Y. Dkhissi, Y. Zhu, J. Etheridge, A. Gray-Weale, U. Bach, Y.-B. Cheng, L. Spiccia, *Angew. Chem. Int. Ed.* **2014**, *53*, 9898.
[20] N. J. Jeon, J. H. Noh, Y. C. Kim, W. S. Yang, S. Ryu, S. I. Seok, *Nat. Mater.* **2014**, *13*, 897.
[21] J. M. Frost, K. T. Butler, F. Brivio, C. H. Hendon, M. van Schilfgaarde, A. Walsh, *Nano Lett.* **2014**, *14*, 2584.
[22] J. M. Frost, K. T. Butler, A. Walsh, *APL Mater.* **2014**, *2*, 081506.
[23] W. Zhang, M. Saliba, D. T. Moore, S. K. Pathak, M. T. Hörantner, T. Stergiopoulos, S. D. Stranks, G. E. Eperon, J. A. Alexander-Webber, A. Abate, A. Sadhanala, S. Yao, Y. Chen, R. H. Friend, L. A. Estroff, U. Wiesner, H. J. Snaith, *Nat. Commun.* **2015**, *6*, 6142.
[24] M. Saliba, K. W. Tan, H. Sai, D. T. Moore, T. Scott, W. Zhang, L. A. Estroff, U. Wiesner, H. J. Snaith, *J. Phys. Chem. C* **2014**, *118*, 17171.
[25] K. W. Tan, D. T. Moore, M. Saliba, H. Sai, L. A. Estroff, T. Hanrath, H. J. Snaith, U. Wiesner, *ACS Nano* **2014**, *8*, 4730.
[26] D. B. Mitzi, S. Wang, C. A. Feild, C. A. Chess, A. M. Guloy, *Science* **1995**, *267*, 1473.
[27] I. E. Rauda, R. Senter, S. H. Tolbert, *J. Mater. Chem. C* **2013**, *1*, 1423.
[28] F. Huang, Y. Dkhissi, W. Huang, M. Xiao, I. Benesperi, S. Rubanov, Y. Zhu, X. Lin, L. Jiang, Y. Zhou, A. Gray-Weale, J. Etheridge, C. R. McNeill, R. A. Caruso, U. Bach, L. Spiccia, Y.-B. Cheng, *Nano Energy* **2014**, *10*, 10.
[29] Q. Chen, H. Zhou, Z. Hong, S. Luo, H.-S. Duan, H.-H. Wang, Y. Liu, G. Li, Y. Yang, *J. Am. Chem. Soc.* **2014**, *136*, 622.
[30] Y. Tidhar, E. Edri, H. Weissman, D. Zohar, G. Hodes, D. Cahen, B. Rybtchinski, S. Kirmayer, *J. Am. Chem. Soc.* **2014**, *136*, 13249.
[31] C. R. McNeill, H. Ade, *J. Mater. Chem. C* **2013**, *1*, 187.
[32] J. Stöhr, *NEXAFS Spectroscopy*, Springer, Berlin, Germany **1992**.
[33] J. Rivnay, S. C. B. Mannsfeld, C. E. Miller, A. Salleo, M. F. Toney, *Chem. Rev.* **2012**, *112*, 5488.
[34] J. M. Ball, M. M. Lee, A. Hey, H. J. Snaith, *Energy Environ. Sci.* **2013**, *6*, 1739.
[35] W. Huang, E. Gann, L. Thomsen, C. Dong, Y.-B. Cheng, C. R. McNeill, *Adv. Energy Mater.* **2015**, *5*, 1401259.
[36] T. Schuettfort, L. Thomsen, C. R. McNeill, *J. Am. Chem. Soc.* **2013**, *135*, 1092.
[37] D. M. DeLongchamp, R. J. Kline, D. A. Fischer, L. J. Richter, M. F. Toney, *Adv. Mater.* **2011**, *23*, 319.
[38] D. T. Moore, H. Sai, K. W. Tan, D.-M. Smilgies, W. Zhang, H. J. Snaith, U. Wiesner, L. A. Estroff, *J. Am. Chem. Soc.* **2015**, *137*, 2350.
[39] J. A. McLeod, Z. Wu, P. Shen, B. Sun, L. Liu, *J. Phys. Chem. Lett.* **2014**, *5*, 2863.
[40] B. Watts, L. Thomsen, P. C. Dastoor, *J. Electron Spectrosc. Relat. Phenom.* **2006**, *151*, 105.
[41] M. Xiao, F. Huang, W. Huang, Y. Dkhissi, Y. Zhu, J. Etheridge, A. Gray-Weale, U. Bach, Y.-B. Cheng, L. Spiccia, *Angew. Chem. Int. Ed.* **2014**, *53*, 9898.
[42] N. M. Kirby, S. T. Mudie, A. M. Hawley, D. J. Cookson, H. D. T. Mertens, N. Cowieson, V. Samardzic-Boban, *J. Appl. Crystallogr.* **2013**, *46*, 1670.
[43] J. Ilavsky, *J. Appl. Crystallogr.* **2012**, *45*, 324.
[44] B. C. C. Cowie, A. Tadich, L. Thomsen, *AIP Conf. Proc.* **2010**, *1234*, 307.